PAPER

Check for updates

Electrochemical evaluation of anodic galvanized-iron nanoparticles as electrode materials for supercapacitors

Muhammad Haseem Bhatti,[a] Muhammad Danish,[a] Jawad Ahmad,[a] Wasif Ali,[b] Maaz Khan, [ID][a] Mashkoor Ahmad, [ID][a] Ghafar Ali, [ID] *[a] Muhammad Nadeem,[c] Nasir Mehboob[d] and Imran Shakir[e]

Electrode materials with excellent electrochemical features are essential for high-performance supercapacitors (SCs). This study explores galvanized iron (GI), a low-cost and naturally abundant material, as an innovative electrode platform for SC applications. GI (zinc coated iron) was anodized in an environmentally benign electrolyte, which produced α-Fe$_2$O$_3$ nanoparticles (NPs). The structural and compositional properties of the α-Fe$_2$O$_3$ material were investigated using X-ray diffraction (XRD), inductively coupled plasma optical emission spectroscopy (ICP-OES), scanning electron microscopy (SEM), high resolution transmission electron microscopy (HRTEM), Fourier-transform infrared spectroscopy (FTIR), and X-ray photoelectron spectroscopy (XPS). The electrochemical performance was evaluated through cyclic voltammetry (CV), galvanostatic charge–discharge (GCD), and electrochemical impedance spectroscopy (EIS). The anodic GI electrode demonstrated enhanced electrochemical kinetics and achieved a high specific capacitance (C_s) of 694 F g^{-1} at a current density of 2 A g^{-1}, significantly higher than the pure anodic iron oxide NPs. An asymmetric supercapacitor (ASC) device assembled from anodic GI (α-Fe$_2$O$_3$) NPs as the positive electrode and activated carbon (AC) as the negative electrode delivered a C_s of 132 F g^{-1} at 2 A g^{-1}, with an energy density of approximately 22.18 Wh kg^{-1} at a power density of $\sim$1093 W kg^{-1}. Notably, the device retained $\sim$94% of its initial capacitance after 7000 charge–discharge cycles, demonstrating excellent long-term stability.

1. Introduction

With the increasing demand for sustainable energy and the decline in fossil fuel usage, researchers are intensively focused on developing advanced and efficient energy storage systems.[1–3] Among various energy storage systems, SCs have been considered the most cutting edge energy storage technology because of their exceptional cyclic stability, high power density, environmental friendliness, and quick charge/discharge cycles.[4,5] They can be classified into two main types based on their charge storage mechanism: (1) electric double layer capacitors (EDLCs) store energy electrostatically at the interface of the electrodes and the electrolyte. In this type of SC, there is no electron exchange and no redox reaction and hence the energy is stored non-faradaically. (2) Pseudocapacitors, also known as redox electrochemical capacitors, derive their capacitance from faradaic reactions occurring at the electrode/electrolyte interface. In this type of SCs, electron transfer and redox reactions take place. Carbon-based materials are used for EDLCs while transition metal oxides (TMOs) and conducting materials are used for pseudocapacitors.[6–8] To date, various TMOs including NiO, ZnO, Cr$_2$O$_4$, SnO$_2$, RuO$_2$, Co$_3$O$_4$, and MnO$_2$[9–15] have been used as electrode materials for SCs. Among them, iron-oxide is considered the most promising electrode material due to its low cost, abundant availability, non-toxicity, and ease of synthesis into different morphologies. However, its low capacitance value and poor electrical conductivity affect its performance for SC applications.[16] In order to overcome this problem GI, a zinc-coated iron material commonly used in structural and corrosion resistant applications, is emerging as a promising substrate for energy storage devices. Its wide availability, mechanical robustness, cost effectiveness, corrosion resistance, high C_s, and electrical conductivity make it an attractive platform for the development of flexible and binder free SC electrodes.[17,18]

[a] *Nanomaterials Research Group, Physics Division, PINSTECH, Islamabad 45650, Pakistan. E-mail: ghafarali@kaist.ac.kr, ghafarali@gmail.com*

[b] *Department of Physics, Abdul Wali Khan University Mardan, KPK, Pakistan*

[c] *Nuclear Engineering Division, PINSTECH, Islamabad 45650, Pakistan*

[d] *Ripah International University, Islamabad, Pakistan*

[e] *Department of Physics, Faculty of Science, Islamic University of Madinah, Madinah 42351, Saudi Arabia*

Up to now, various methods have been attempted for the synthesis of pure iron-oxide NPs, such as hydrothermal processes,[19] co-precipitation,[20] sol–gel processes,[21] and electrodeposition,[22] *etc.* However, these methods have notable drawbacks such as being time consuming, requiring a high temperature for reaction, and low purity yields. These limitations negatively impact the performance and result in unsatisfactory capacitance, which restricts their practical application in SCs. On the other hand, the anodization method is an electrochemical process that transforms metals and alloys into their oxide NPs, depending on the type of electrolyte used during the process. It offers several advantages over other methods used for preparing metal–oxide NPs as described in our previous article.[23] It is very simple, affordable, environmentally friendly and time-efficient, and produces a highly pure product at room temperature in a single-step process.

The key objective of the present work is to develop an electrode material with large C_s, high power and high energy density, and good cycling stability. In this regard, for the first time, anodic GI-oxide NPs are produced by a facile anodization technique and their SC performance is compared with pure iron-oxide NPs obtained under similar conditions *via* anodization. The developed anodic GI electrode exhibits a high C_s and energy density, and excellent stability compared to the pure iron-oxide NP electrode. These results make the anodic GI electrode a potential candidate for next-generation electrochemical energy storage devices.

## 2. Experimental

2.1. Materials and chemicals

Galvanized iron sheet ($\sim$0.12 μm thick), pure iron sheet (99.99% pure), and nickel foam (0.5 mm thick) were purchased from ZHIJI Metal, China. Reagent-grade sodium chloride (NaCl, 99.99% pure), potassium hydroxide (KOH, 99.99% pure), sulfuric acid (H_2SO_4, 98% pure), acetone, and ethanol were sourced from Sigma-Aldrich, USA. Carbon black (99.99% pure) and activated carbon (AC) were bought from XINGNUO, China. Poly(vinylidene fluoride-*co*-hexafluoropropylene) (PVDF-HFP) and *N*-methylpyrrolidone (NMP) were acquired from Alfa Chemistry, USA. Deionized (DI) water was used to prepare the electrolyte.

2.2. Anodization of sheets

Before anodization, GI and iron sheets were washed by sonicating in acetone, ethanol, and DI water each for five minutes and then kept in an oven for drying at 60 °C. According to the schematic in Fig. S1, anodization was carried-out in a home-made two-electrode setup using a GI/iron sheet as the anode and a platinum plate ($15 \times 25 \times 0.2$ mm^3) as the cathode. Anodization was performed separately for both sheets at room temperature in 1 M aqueous NaCl electrolyte at constant voltage (10 V) using a programmable DC power supply (Tektronix PWS 4305, USA). When the power supply was turned-on, precipitates began to form from the GI sheet (anode electrode), and a strong evolution of H_2 gas at the cathode (Pt plate) was

observed according to the chemical eqn (2.6). The entire GI sheet was transformed into solid precipitates, which settled down at the bottom of the beaker with anodization time. Thus, in a 1 M NaCl electrolyte, the anodization process completely transformed the GI and iron sheets into their respective oxide powder. The resulting precipitates were initially dispersed and sonicated in DI water using an ultrasonic bath (Elma E60H, Germany) for 5 minutes. They were then collected *via* centrifugation to eliminate excess NaCl that may have been acquired from the electrolyte during anodization. This process was performed 7 times to confirm that NaCl salt was completely eliminated from the final product. The precipitates were dried in an oven at 70 °C overnight, and then ground into powder form using a mortar-pestle. The resulting GI-oxide and iron-oxide powder (anodic metal–oxide) was subsequently annealed at 500 °C for 2 hours with a heating rate of 3 °C min^{-1}, and then allowed to cool at room temperature. Similarly, the iron sheet was also anodized under the same conditions and parameters for comparison.
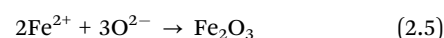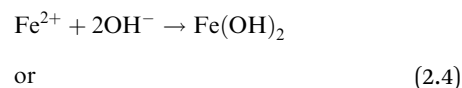
The formation mechanism of the iron-oxide NPs *via* anodization is proposed as follow: iron-oxide NPs produced *via* anodization in NaCl aqueous electrolyte are based on the dissolution of a sacrificial iron sheet as the anode. When potential is applied from the DC power supply, the primary reaction will occur and the anode loses its outermost electrons, which involves the oxidation of iron to iron ions (Fe^{2+} or Fe^{3+}) *via* the following reactions.

$$Fe(s) \rightarrow Fe^{2+}(aq) + 2e^-$$

$$\text{or} \tag{2.1}$$

$$Fe(s) \rightarrow Fe^{3+}(aq) + 3e^-$$
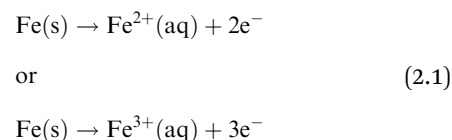
As a result, the anode surface produced cations. The coulombic repulsive force causes the generated cations to drift from the anode surface into the electrolyte. The generation of cations from the sacrificial anode due to the applied voltage and their drifting into the electrolyte solution is a process that occurs continuously. Due to electrolysis of water, anions in the NaCl aqueous solution are produced, resulting in a reduction in thickness of the sheet at the anode with anodizing time *via* the following reaction;

$$H_2O \rightarrow H^+ + OH^- \tag{2.2}$$

$$2OH^- \rightarrow 2H^+ + 2O^- \tag{2.3}$$
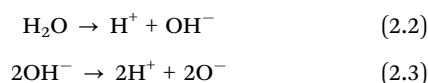
Iron-oxide NPs are produced when metallic cations react with anions present in the electrolyte *via* the following reactions;

$$Fe^{2+} + 2OH^- \rightarrow Fe(OH)_2$$

$$\text{or} \tag{2.4}$$

$$Fe^{3+} + 3OH^- \rightarrow Fe(OH)_3$$

$$2Fe^{2+} + 3O^{2-} \rightarrow Fe_2O_3 \tag{2.5}$$

According to the Nernst equation, the chemical reaction between the cations generated from the sacrificial anode and the electrolyte anion species (OH^- and O^{2-}) is found to be more favorable thermodynamically. During the oxidation of the iron sheet, hydrogen gas is simultaneously rapidly evolved at the cathode *via* the following reaction;

$$4H^+ + 4e^- \rightarrow 2H_2\uparrow \text{ (at the cathode)} \qquad (2.6)$$
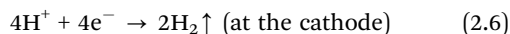
2.3. Preparation of electrodes

The anodic GI electrode was prepared using a mixture of GI oxide NPs (α-Fe_2O_3), carbon black, and poly(vinylidenefluoride-hexafluoropropylene) (PVDF-HFP, serving as a binder) that was prepared in a weight ratio of 70:20:10, with a few drops of *N*-methylpyrrolidone (NMP). The mixture was stirred for 24 hours to achieve a homogeneous slurry. This slurry was then coated ($\sim$1.0 mg) onto the cleaned NF, with an active area of $\sim$0.5 cm^2, and dried in a vacuum oven at 60 °C for 24 hours. Similarly, we prepared an electrode of pure iron-oxide (α-Fe_2O_3) NPs under identical conditions for comparison.

2.4. Fabrication of the ASC GI (α-Fe_2O_3)//activated carbon (AC) device

In order to prepare a device based on anodic GI-oxide NPs (α-Fe_2O_3), AC was used as the negative electrode while GI-oxide NPs were used as the positive electrode. The aforementioned slurry was pasted on a nickel (Ni) sheet (0.1 mm thickness, Goodfellow, England, UK). Meanwhile, a slurry consisting of 75 wt% AC and 25 wt% PVDF-HFP was applied to aluminum foil to prepare the negative electrode for device fabrication. The active material loading on both the positive and negative electrodes is approximately 1 mg and 3 mg respectively, with 1 M KOH employed as the electrolyte. The optimized mass ratio used in the ASC device was 1:3, which provided the best electrochemical performance in terms of specific capacitance, energy density, and cycling stability. For the ASC, Ni-sheet, Al-foil, Whatman filter paper, and 1 M KOH were utilized as the current collector, separator, and electrolyte, respectively. The size of the fabricated device was (1 × 1) cm^2 which was used to glow the commercially available LEDs.

2.5. Characterization

The inductively coupled plasma optical emission spectroscopy (ICP-OES) technique was used to analyze the element composition of the GI-oxide NPs and pure iron-oxide NPs. The prepared samples were investigated using a GAXRD (Rigaku D/MAX 2500 V diffractometer, Japan) *via* Cu Kα source (λ = 1.5418 Å) radiation at 40 kV to determine their crystal structure and phase purity. The surface morphology and elemental composition of the synthesized products were examined by scanning electron microscopy (UHR-SEM Magellan 400, FEI, USA) furnished with energy dispersive spectroscopy (EDS) and TEM (Techni G2 F30, FEI, USA). Oxidation state was determined from X-ray photoelectron spectroscopy (XPS) analysis conducted using a spectrometer (Sigma Probe, Thermo VG Scientific) with an Al Kα excitation

source operated at 15 kV and 7 mA. Fourier-transform infrared (FTIR) spectroscopy was performed by using a Nicolet iS50 FTIR spectrometer. The FTIR spectrum was recorded in the range of 4000–400 cm^{-1}.

2.6. Electrochemical measurements

The electrochemical measurements were performed in a basic aqueous electrolyte (1.0 M KOH) by an electrochemical work-station (CHI660E, China). In a three electrode system, the material deposited on NF acted as a working electrode, a platinum electrode worked as the counter electrode, and a Hg/HgCl$_2$ electrode served as the reference electrode. The cyclic voltammetry (CV) measurements were conducted at various scan rates, ranging from 5 to 50 mV s^{-1} with a voltage window of -0.4 to 0.6 V. Measurements of the galvanostatic charge–discharge (GCD) were carried-out in a voltage window of 0.0 to 0.5 V and current density from 2 to 5 A g^{-1}. EIS measurements were conducted over the frequency range of 0.1 Hz to 140 kHz. All the electrochemical measurements were performed at room temperature. The ASC device was also characterized by CV and GCD in the potential window of 0.0 to 1.1V in 1M KOH electrolyte. Analysis of the ASC device using EIS was carried-out over the frequency range of 100 mHz to 100 kHz. Two-electrode system was used to check the electrochemical performance of the fabricated device. The C_s, energy density (E_d), and power density (P_d) were calculated using the following equations (3.1–3.3):

$$C_s = \frac{I \times \Delta t}{m \times \Delta v} \qquad (3.1)$$

$$E_d = \frac{C_s \times \Delta v^2}{7.2} \qquad (3.2)$$

$$P_d = \frac{3600 \times E_d}{\Delta t} \qquad (3.3)$$

where C_s is the specific capacitance of the active materials, I is the discharging current, m is the mass of the active materials, ΔV represents the discharging potential window, Δt is the discharging time, E_d is the energy density and p_d is the power density. In addition, the coulombic efficiency (η) of the fabricated electrodes was calculated by eqn (3.4):

$$\eta = \frac{T_c}{T_d} \times 100\% \qquad (3.4)$$

where, T_c and T_d are the charging and discharging time in seconds, respectively.

3. Results and discussion

3.1. Inductively coupled plasma optical emission spectrometry (ICP-OES)

The element composition of the anodic GI and pure iron-oxide NPs was determined using ICP-OES analysis and the results are summarized in Table 1. The ICP results clearly show the presence of Zn in the anodic GI-oxide NPs, unlike the pure iron-oxide NPs, which confirms that Zn has been incorporated as a result of GI-sheet anodization. Moreover, Fe is the main

Table 1 ICP-OES results of the anodized GI-oxide NPs and pure iron-oxide NPs

S. no.	Elements	GI sheet	Iron sheet
1	Al	0.027	0.050
2	Cd	0.001	0.001
3	Co	0.001	0.003
4	Cr	0.011	0.018
5	Cu	0.002	0.008
6	Mg	0.006	0.014
7	Mn	0.081	0.093
8	Mo	0.003	0.005
9	Na	0.012	0.022
10	Ni	0.001	0.011
11	P	0.002	0.002
12	S	0.001	0.003
13	Si	0.014	0.018
14	Zn	1.676	0.026
15	Fe	Balance	

constituent element in both the anodic GI and iron-oxide NPs, along with other elements present in trace amounts. Compared to the anodic GI-oxide NPs, the pure iron oxide NPs have very low Zn content in trace amounts, which confirms that it is not coated with Zn like the GI.

3.2. Structural analysis

XRD was performed to evaluate the crystal structure of the prepared samples and is shown in Fig. 1(a). It can be seen that the XRD patterns of the GI-oxide NPs and iron-oxide NPs show distinct and well defined peaks observed at ∼24.16°, 33.12°, 35.61°, 40.89°, 49.48°, 54.01°, 62.37°, 63.96°, 72.04°, and 75.20°, which can be attributed to the (012), (104), (110), (113), (024), (116), (214), (300), (119), and (220) planes of α-Fe$_2$O$_3$ (ICDD card # 01-079-1741), respectively. All the identified peaks belong to the hematite phase of α-Fe$_2$O$_3$. In addition, the peaks of pure iron-oxide NPs are relatively sharp compared to the diffraction peaks of the GI-oxide NPs (zoomed-in view of Fig. 1(b)). The full width at half maximum (FWHM) values of the (104) plane of the anodic GI-oxide and iron oxide NPs are 0.1982 and 0.1950, respectively. The Zn peak in the XRD pattern of the GI-oxide NPs is not detected because the zinc layer on the iron surface is quite thin, typically in the range of a few microns (10–20 μm).

XRD is a bulk characterization technique, which means that the X-rays penetrate into the substrate material. As a result, the diffraction signal from the much thicker iron substrate can dominate and overshadow the weaker signal from the zinc layer.[24] No additional peaks of impurities are observed in the XRD patterns, indicating the high purity of the samples.

3.3. Morphology analysis and composition

The surface morphology and composition of GI-oxide and iron-oxide NPs were examined using SEM, as depicted in Fig. 2. Fig. 2(a) and (b) show the low and high magnification images of the pure iron-oxide NPs. These particles appeared to have adequate porosity and were predominantly quasi-spherical with slight variation in their size and shape. These NPs tend to cluster together at some area, forming agglomerates. These agglomerates are composed of small particles that might stick to each other due to van der Waals forces.[25] The bar graph in Fig. S2(a) depicts the particle size distribution of the pure iron-oxide NPs, with an average particle size of approximately 45.56 nm. The distribution is relatively narrow with most of the particles falling within the 45–50 range. Fig. 2(c) shows the EDX spectrum of the pure iron-oxide NPs. It identifies iron (Fe) as the predominant element alongside minor peaks for oxygen (O) and carbon (C). The morphology of the GI-oxide NPs shown in Fig. 2(d) and (e) closely resembles that of the pure iron-oxide NPs but they differ slightly in particle size. The size of the GI-oxide NPs is relatively high as shown in the high magnification image (Fig. 2d). This may be attributed to the Zn coating on Fe.[26] The EDX spectrum (Fig. 2(f)) confirms that iron (Fe) is the main element in the GI oxide NPs as well besides the notable peaks of O and Zn. The EDX results align well with the XRD results, confirming that the prepared samples are free of impurities. Fig. S2(b) illustrates the particle size distribution of the GI-oxide NPs showing a slightly large average particle size of ∼49.34 nm and a broader range, indicating greater variability likely due to the presence of Zn in the GI-oxide NPs.

High-resolution transmission electron microscopy (HRTEM) was used to further investigate the structural morphology of the prepared samples. Fig. 3a shows the low-resolution TEM image
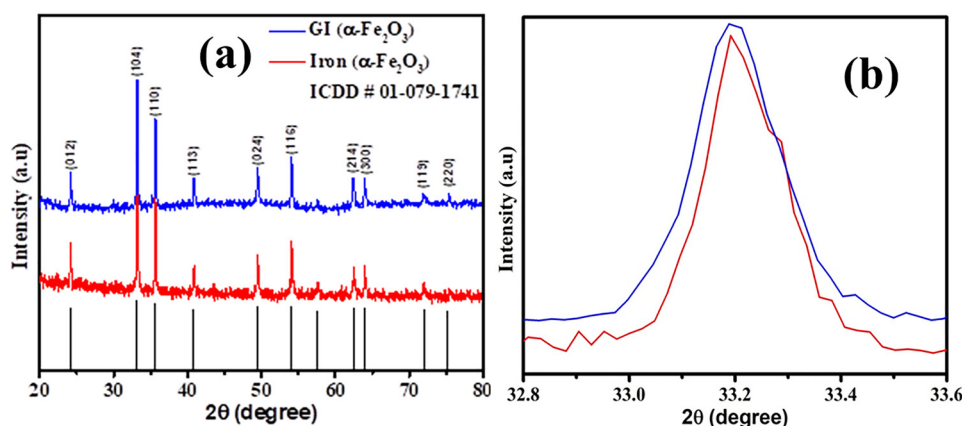
Fig. 1 XRD patterns of the (a) GI-oxide NPs and the pure iron-oxide NPs and (b) zoomed in view of the overlapping peaks.
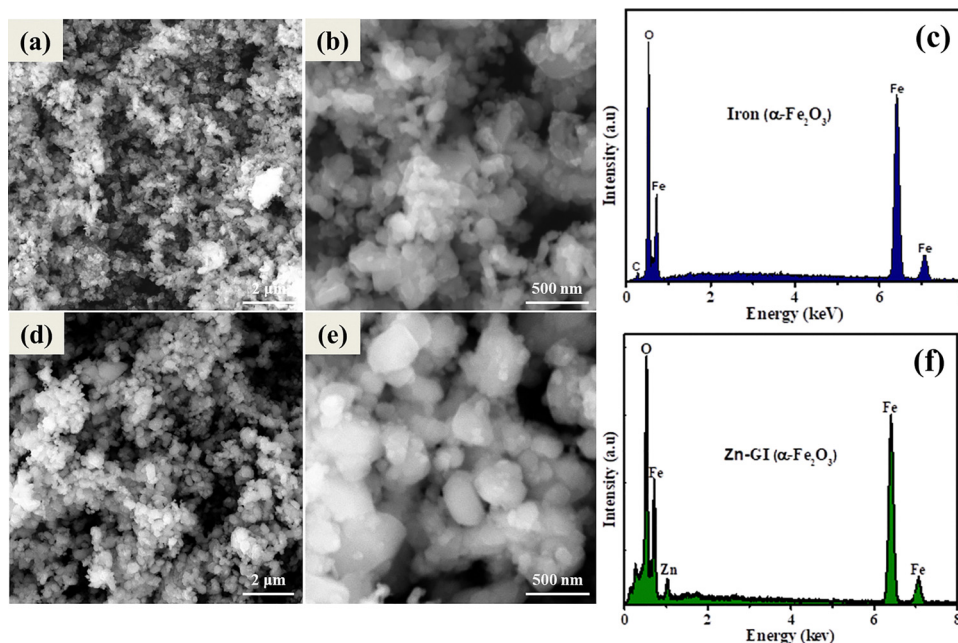
Fig. 2 The (a) low and (b) high magnification SEM images of the pure iron-oxide NPs along with (c) the EDX spectrum, and (d) and (e) shows the low and high magnification SEM images of the GI-oxide NPs with (f) the EDX spectrum.

of the pure iron-oxide NPs, which exhibits that the quasi spherical nature further verifies the SEM results. Fig. 3b reveals the high-resolution TEM image of the pure iron-oxide NPs. It clearly displays the grain boundaries of the particles and lattice fringes with a spacing of 0.27 nm and 0.26 nm, corresponding to the (101) and (110) crystal planes of Fe_2O_3, respectively. These well-defined fringes indicate the good crystallinity of the pure iron-oxide NPs after calcination. Similarly, Fig. 3c

Fig. 3 TEM images (a) and (b) of the pure iron-oxide (Fe_2O_3) NPs and (c) and (d) GI-oxide NPs.

depicts the low-resolution TEM image of the GI-oxide NPs, showing that these NPs are almost similar to the pure iron-oxide NPs but larger in size than the iron oxide nanoparticles, which is also in good agreement with the SEM results (2e). Fig. 3d demonstrates the HRTEM image of the GI-oxide NPs having similar lattice fringes with a spacing of 0.26 nm corresponding to the (110) plane of the α-Fe_2O_3 phase. However, the fringes may appear slightly less distinct or more disordered compared to the pure iron oxide, suggesting that the Zn coating affects the crystal structure and showing the amorphous structure.

XPS measurement was conducted to investigate the electronic structure and chemical composition of the prepared GI-oxide NPs. As evidenced from the XPS survey spectrum in Fig. 4(a), the GI-oxide NPs reveal the peaks of Fe, O, and Zn, confirming the expected elemental composition of the anodized GI oxide NPs. Fig. 4(b) displays that the deconvoluted spectrum of Fe 2p at about 710.1 eV and 723.5 eV binding energy is assigned to the electronic states of the Fe $2p_{3/2}$ and Fe $2p_{1/2}$ spin orbit doublet, respectively, with an energy separation of 13.4 eV, consistent with the literature, confirming the oxidation states (Fe^{3+}) of iron in our sample.[27] Furthermore, the presence of a satellite peak at $\sim$718.4 eV confirms the existence of the hematite phase. The high resolution spectrum of the Zn 2p peaks is shown in Fig. 4(c). It is seen that two prominent peaks are observed at 1022.2 eV and 1045.4 eV, which correspond to Zn $2p_{3/2}$ and Zn $2p_{1/2}$, respectively, with a spin energy separation of 23.2 eV, consistent with the characteristic divalent state of zinc (Zn^{2+}).[28] Fig. 4(d) illustrates the high resolution spectrum of the O 1s peak. A prominent peak is observed at 528.7 eV, indicating the presence of lattice oxygen (O^{-2}) in the hematite (α-Fe_2O_3).[29] The XPS spectra exhibit distinct peaks
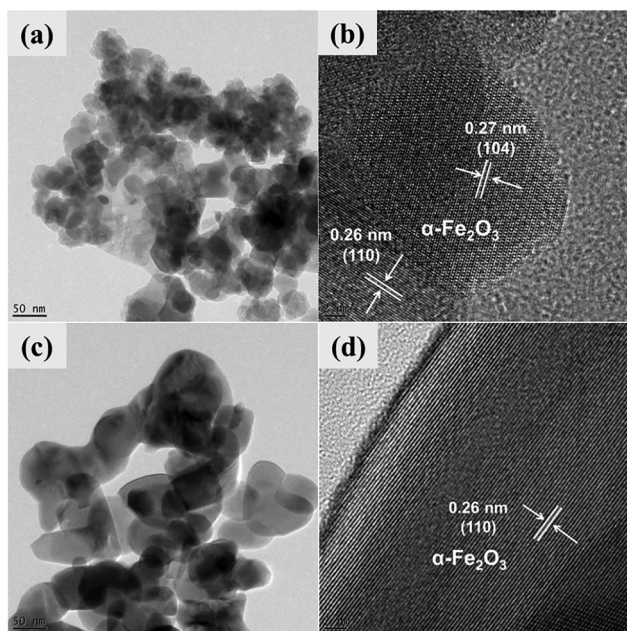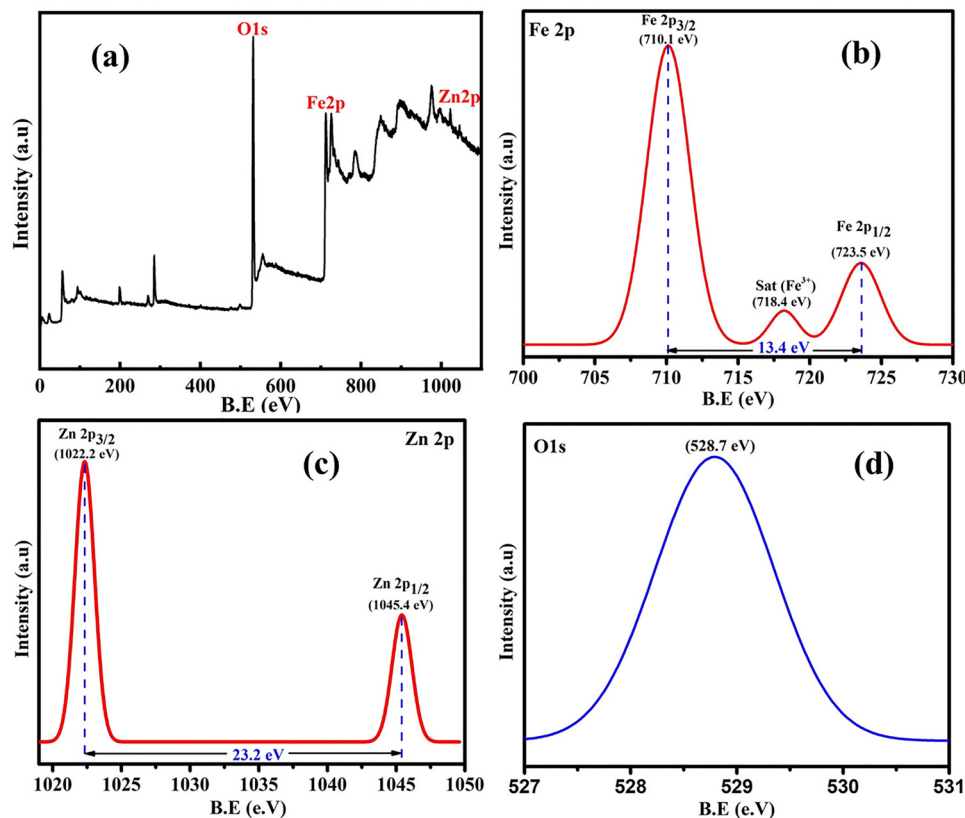
Fig. 4 XPS analysis of the GI oxide NPs: (a) survey spectrum and high resolution spectra of (b) Fe 2p, (c) Zn 2p, and (d) O 1s.

corresponding to Zn and O, confirming the presence of ZnO in the sample. This observation is further supported by the EDX analysis, which also indicates the coexistence of zinc and oxygen elements, thereby validating the successful formation of ZnO. This binding energy is characteristics of an oxygen atom strongly bonded to iron (Fe–O) in a crystalline lattice, which is a key feature of the hematite electronic structure.

3.4. Fourier transform infrared spectroscopy (FTIR)

FTIR spectra of the GI-oxide NPs and the pure iron-oxide NP structures were recorded in the range of 4000 to 400 cm^{-1} as depicted in Fig. S3. Sharp peaks were observed at 463, 518, and 911 cm^{-1} for the GI-oxide NPs and 434, 524, and 928 cm^{-1} for the iron-oxide NPs corresponding to the Fe–O bond. An additional peak at 429 cm^{-1} in the GI-oxide NPs is attributed to the Zn–O bond, influenced by the presence of Zn in the GI-oxide NPs. These are characteristic of metal–O bonds,[30] confirming the formation of α-Fe_2O_3. The broad peak at 3521 cm^{-1} for the GI-oxide NPs and the sharp peak at 3745 cm^{-1} for the iron-oxide NPs are associated with the stretching vibration of the OH group.[31] These FTIR results are compatible with the XRD and EDX data.

3.5. Electrochemical performance of the fabricated electrode

3.5.1. Cyclic voltammetry (CV). The electrochemical performance of the GI-oxide NP electrode and iron-oxide NP electrode was evaluated using CV measurements at different scan rates, ranging from 5 to 50 mV s^{-1} within a potential window range of −0.4 to 0.6 V. Fig. 5a presents the CV comparison between the GI-oxide electrode and the iron-oxide electrode at a scan rate of 30 mV s^{-1} within the potential window of −0.4 to 0.6 V. The GI-oxide electrode exhibits a significantly larger enclosed area under the CV curve compared to the iron-oxide electrode, indicating a good pseudo-capacitance behavior, reversibility, enhanced electrochemical activity, and higher charge storage capacity.

Fig. 5b illustrates the CV curves of the GI-oxide electrode recorded at various scan rates ranging from 5 to 50 mV s^{-1} within the potential window of −0.4 to 0.6 V. As the scan rate increases, the current response also increases progressively, showing a good rate capability and electrochemical reversibility of the electrode material. The increasing area under the curves at higher scan rates reflects an enhancement in the charge storage capability due to fast ion diffusion. However, the relatively small peak shifts indicate efficient charge transfer and minimal resistive losses.[32] Redox peaks are also clearly seen for different scan rates, confirming the pseudo-capacitive nature of the GI-oxide electrode. Similarly, the CV curves of the pure iron-oxide electrode in Fig. S4(a) show similar behavior under the same scan rates and potential window. However, the area under the curves is smaller compared to the GI-oxide electrode. Although the current response increases with increasing scan rate, the overall charge storage capability is lower than that of the GI-oxide electrode.
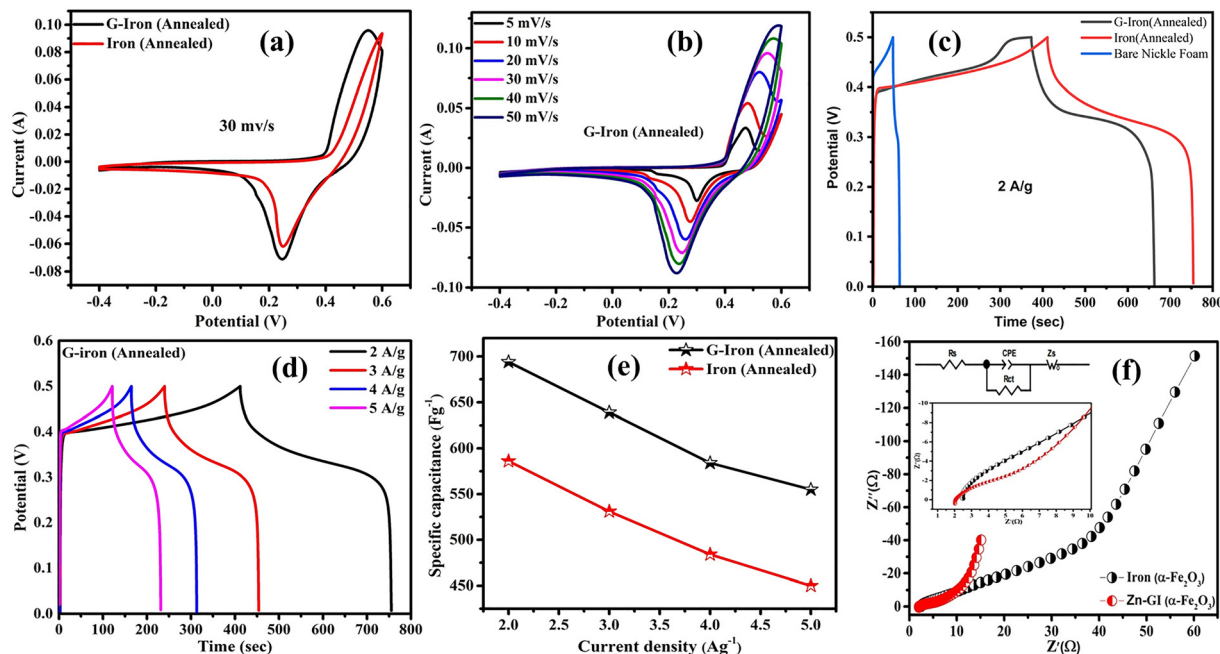
Fig. 5 Electrode performance: (a) comparative CV response of the GI oxide NPs and iron-oxide NPs electrodes at a scan rate of 30 mV s^{-1}; (b) CV response of the GI oxide NPs electrode at a scan rate of 5, 10, 20, 30, 40, and 50 mV s; (c) comparison of the GCD curve of the GI oxide NPs and iron-oxide NPs electrodes and bare nickel foam at a current density of 2 A g^{-1}; (d) GCD curves of the GI oxide NPs electrode at a current density of 2, 3, 4, and 5 A g^{-1}; (e) comparison of C_s at different current densities with the reported work; (f) Nyquist plot of the GI oxide NPs and iron-oxide NPs electrodes; insets are the kinetic parameters of both electrodes.

3.5.2. Galvanostatic charge–discharge of the Zn-GI electrode. Galvanostatic charge–discharge (GCD) measurements were also used to further assess the electrochemical performance of the GI-oxide and pure iron-oxide electrodes. Fig. 5c displays the comparison between the GI-oxide electrode and iron-oxide electrodes at a current density of 2 A g^{-1}. Both electrodes exhibit non-linear charge–discharge profiles, which is indicative of pseudocapacitive behavior. Furthermore, bare nickel foam was also compared with the GI-oxide and pure iron-oxide electrode at a current density of 2 A g^{-1}. The nickel foam exhibited a nearly linear curve with a very short discharge time as compared to GI-oxide and pure iron-oxide electrodes, confirming its negligible capacitance contribution within the tested potential window. Therefore, the specific capacitance values reported were calculated solely based on the mass of the active material, without including nickel foam.

The GI-oxide electrode demonstrates a longer discharge time as compared to the iron-oxide electrode, which reflects its higher C_s and great charge storage capability due to the synergistic effect of Fe and Zn. However, a clear difference in the performance is observed between the two electrode materials. This improved performance of the GI-oxide electrode can be attributed to the incorporation of Zn, which enhances the electrical conductivity, improves electron transport, and provides a larger surface area for ion interaction. Fig. 5d displays the GCD curves of the GI-oxide electrode at various current densities, ranging from 2 to 5 A g^{-1}. The calculated C_s values are 694, 639, 584, and 555 F g^{-1} at a current density of 2, 3, 4, and 5 A g^{-1}, respectively. The GI-oxide electrode achieved the highest C_s of ~694 F g^{-1} at a current density of 2 A g^{-1}, and maintains its capacitance of 555 F g^{-1} at 5 A g^{-1}. In comparison, the pure iron-oxide electrode achieved a C_s of 586, 531, 484, and 450 F g^{-1} under the same current densities, reaching a maximum C_s of 586 F g^{-1} at 2 A g^{-1} and retaining 450 F g^{-1} at 5 A g^{-1} (Fig. S4(b)). The GCD curves maintain a consistent shape across different current densities, confirming the excellent stability of the fabricated electrode and further validating the CV results. In addition, from the GCD curves we can see that the C_s of the electrode decreases as the current density increases. This is because, at higher current densities, the movement of the electrolyte ions becomes less correlated with the rate of current flow.[32] It can be clearly seen that the GI-oxide electrode has a superior performance as compared to the pure iron-oxide previous reported electrodes as shown in Table 2.

Fig. 5e illustrates the relationship between the electrode C_s and current densities of the GI-oxide electrode in comparison to the pure iron-oxide and other iron-based electrodes. The graphs clearly showed the enhanced performance of the GI-oxide electrode in comparison with the literature. Energy density and power density are the two most essential parameters in establishing the viability of the electrode material for commercial use. GCD curves were used to compare the energy density and power densities of the GI-oxide electrode and iron-oxide electrode. Table S1, shows that the GI-oxide electrode achieves a high energy density of 24.09 Wh kg^{-1} at a power density of 252.8 W kg^{-1} at 2 A g^{-1}. In comparison, the iron electrode delivers a slightly lower energy density of 20.34 Wh kg^{-1} and a power density of 252.4 W kg^{-1} at the same current density.

**Table 2** Comparative analysis of the C_s and energy density of the fabricated electrode with the reported α-Fe$_2$O$_3$-based electrodes

Materials	Specific capacitance (F g^{-1})	Current density (A g^{-1})	Energy density (Wh g^{-1})	Cycling stability (%)	Cycles numbers	Ref.
Fe$_2$O$_3$	274	1	38.05	75.3	100 000	37
Fe$_2$O$_3$ nanotube	138	1	215.62	89	500	38
NG/Fe$_2$O$_3$	260	2	36.12	82.5	1000	39
N-rGO/Fe$_2$O$_3$	268	2	37.22	95.7	2000	40
α-Fe$_2$O$_3$	127	1	—	98	1000	41
α-Fe$_2$O$_3$	193	1	—	92	1000	42
Iron (α-Fe$_2$O$_3$)	586	2	20.34	—	—	This work
Zn-GI (α-Fe$_2$O$_3$)/NF	694	2	24.09	94	7000	This work

3.5.3. Electrochemical impedance spectroscopy (EIS). The electrode kinetics and charge transfer mechanism are analyzed using electrochemical impedance spectroscopy (EIS), from 100 mHz to 100 kHz in a neutral 1M KOH electrolyte solution. Fig. 5(f) presents the comparative Nyquist plots of the Zn-GI electrode and iron electrode along with an inset fitted equivalent circuit that defines the Nyquist plot parameters. The Nyquist plot consists of three distinct regions: an intercept on the real axis, representing the solution resistance (R_s), a semi-circle in the high frequency region corresponding to the charge transfer resistance (R_{ct}) at the electrode–electrolyte interface, and a sloping line in the low frequency region indicating the Warburg impedance (Z_w), which is related to ion diffusion within the electrolyte. The R_s values of the Zn-GI and iron electrodes are 2.02 Ω and 2.5 Ω, respectively, which are calculated from the intersection of the curve in the real impedance
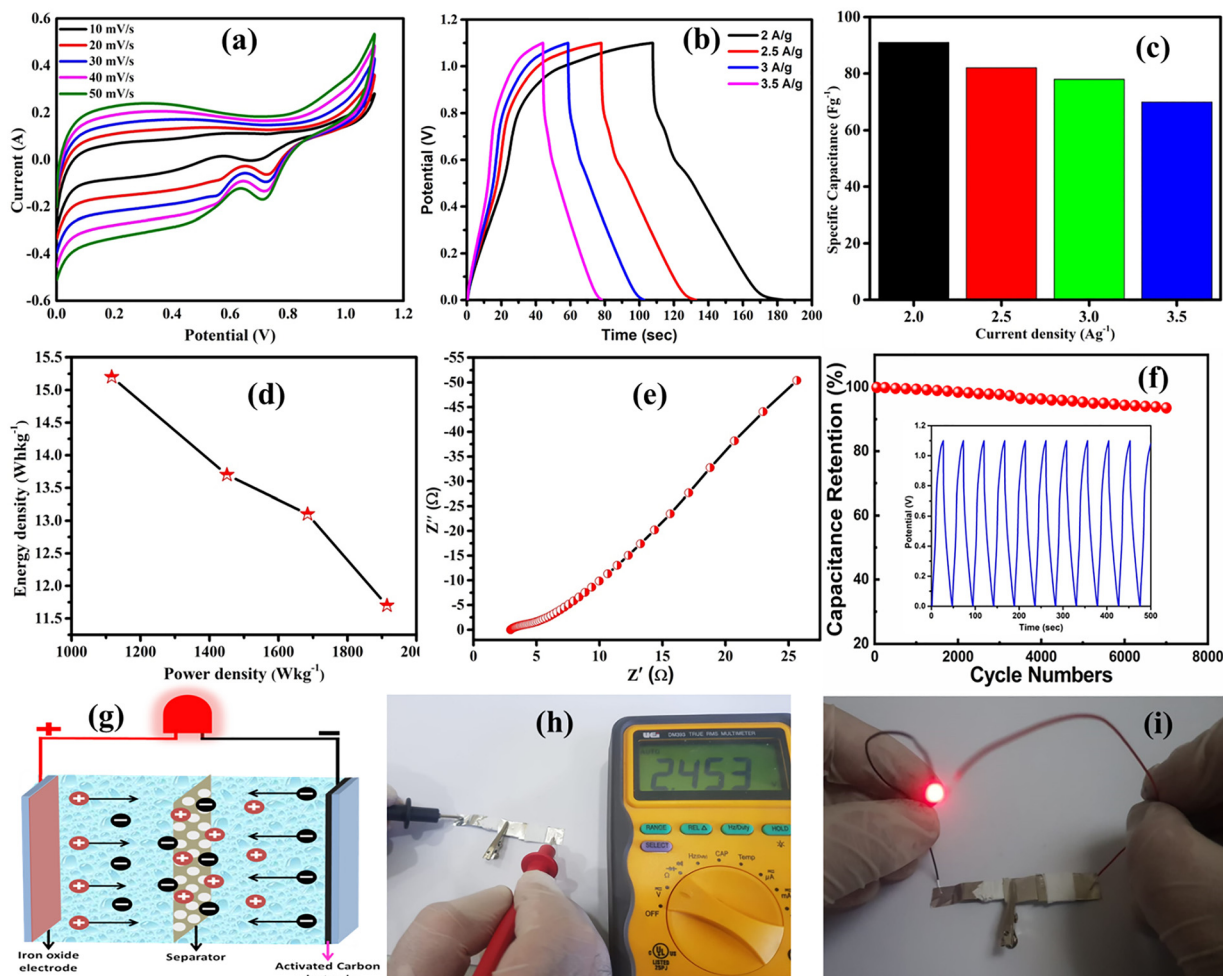
Fig. 6 The GI oxide NPs//AC device performance: (a) CV response at different scan rates; (b) GCD curves at various current rates; (c) the variation of C_s as a function of current density; (d) Ragone plot; (e) Nyquist plot; (f) the C_s retention of Zn-GI//AC at a current density of 8 A g^{-1} (inset shows the charge discharge curves for the first 10 cycles). (g) Shows the inner side mechanism of the device, (h) displays the device voltage and (i) shows the device lighting up a red LED light.

axis Z'. The R_{ct} values of the Zn-GI and iron electrodes are 5.29 Ω and 35.8 Ω, respectively, which are obtained from the semicircle diameter. The small resistance values of the Zn-GI electrode show that it has low internal resistance, excellent conductivity, and a high charge/discharge process at the electrode–electrolyte interface. The increased kinetics of the Zn-GI NPs contribute to the enhanced performance of the electrode. The performance of the Zn-GI electrode was also compared with previously reported iron-based electrodes.

3.5.4. Performance of the (GI-oxide NPs//AC) SC device. The performance of the device was evaluated by recording the CV profiles of the devices at scan rates from 10 to 50 mV s^{-1} within a stable potential window of 0.0 to 1.1 V (Fig. 6a). The current response increased with higher scan rates while maintaining the characteristic shape of the curves. This demonstrates the device's excellent capacitive behavior, as the shape retention confirms its rapid and reversible charge storage capabilities.

Fig. 6(b) shows the GCD curves at different voltage windows ranging from 0 to 1.1 V. The triangular shaped curves at various current densities ranging from 2 to 3.5 A g^{-1} illustrate the high coulombic efficiency with reversibility. The C_s of the device is calculated from the GCD curves at various current densities, as shown by the bar graph in Fig. 6(c). It is observed that the device achieved a high C_s of 132 F g^{-1} at 2 A g^{-1}, that was maintained at 104 F g^{-1} at 3.5 A g^{-1}. The asymmetric triangular shape of the GCD curves highlights the perfect pseudocapacitance behavior of the rapid charge/discharge process. Fig. 6(d) shows the Ragone plot of the ASC device. In a stable voltage window of 0 to 1.1 V, the device performance shows an impressive energy density of 22.18 Wh kg^{-1} at a power density of 1093 W kg^{-1}. It is observed that the device exhibits outstanding performance, delivering a high energy density of 22.18 Wh kg^{-1} at a power density of 1093 W kg^{-1} within a stable voltage window of 0–1.1 V, which is superior to many reported α-Fe$_2$O$_3$ based devices such as C-Fe$_2$O$_3$ (43.5 F g^{-1} and 9.1 Wh kg^{-1}),[33] NCFCO//AC (40 F g^{-1} and 14.2 Wh kg^{-1}),[34] α-Fe$_2$O$_3$@C//MnO$_2$ (55.12 F g^{-1} and 11.94 Wh kg^{-1}),[35] and MnO$_2$//Fe$_2$O$_3$ (92 F g^{-1} and 19.4 Wh kg^{-1}).[36]

Fig. 6(e) presents the Nyquist plot of the device and reveals improved kinetics parameters. The cycling stability is further observed by measuring the GCD curves for 7000 cycles, as shown in Fig. 6(f). It can be seen that the device exhibits outstanding stability with a capacity retention of 94% after 7000 cycles. The inset shows the cyclic stability for the last 22 cycles at a current density of 8 A g^{-1}.

For practical applications, two fabricated devices were connected in series, producing an output voltage of 2.4 V, as shown in Fig. 6(h). When connected to a red LED, the device successfully powered it, resulting in visible light emission, as depicted in Fig. 6(i). All the results demonstrate excellent efficiency, reversibility, and good rate capability of the device.

Conclusion

In summary, this study highlights galvanized iron (GI) as a low cost and widely available material that can be effectively used as an electrode for supercapacitors. Structural and surface analysis confirmed the formation of GI-oxide NPs. The fabricated electrode achieves a high C_s of 694 F g^{-1} at 2 A g^{-1} with good reversibility. The developed asymmetric SC device delivered a C_s of 132 F g^{-1}, with an energy density of 22.18 Wh kg^{-1}, at a power density of 1093 W kg^{-1}. Most importantly, the device showed excellent cycling stability, maintaining about 94% of its initial capacitance after 7000 cycles. These results demonstrate that Zn-GI has strong potential as an efficient and economical electrode material for future energy storage devices.

Author contributions

G. A. conceived the idea, M. H. B., J. A., and M. D. designed the study and carried-out the experiments, W. F. and M. N. helped in characterization and results interpretations. G. A., M. H. B., J. A., and M. D. analyzed the experimental data along with its interpretations. M. H. B., J. A., and M. D. prepared the initial draft of the manuscript. M. A., M. K., N. M., and I. S. revised the initial draft and helped in its improvement by their technical contributions. G. A. funded the study and supervised the project. All authors were involved in the discussion and write up of the manuscript. M. H. B. and G. A. finalized the revised manuscript with inputs and comments from all authors.

Conflicts of interest

No financial conflicts of interest are declared by the authors.

Data availability

The data supporting this article have been included in the main text of the manuscript as well as in the supplementary information (SI). Supplementary Information contain the schematic diagram of metal–oxides NPs preparation, histograms of iron-oxide and GI-oxide NPs, FTIR of iron-oxide and GI-oxide NPs, CV, GCD the pure iron-oxide NPs, and electrochemical measurements comparative table of GI oxide and pure iron-oxide. Supplementary information is available. See DOI: https://doi.org/10.1039/d5ma01224d.

Acknowledgements

References

1 J. Ma, *et al.*, Multifunctional Prussian blue/graphene ink for flexible biosensors and supercapacitors, *Electrochim. Acta*, 2021, **387**, 138496.

2 Y. Ping, *et al.*, N-self-doped graphitic carbon aerogels derived from metal–organic frameworks as supercapacitor electrode materials with high-performance, *Electrochim. Acta*, 2021, **380**, 138237.

3 Z. Wang, *et al.*, Nanosheets based mixed structure $CuCo_2O_4$ hydrothermally grown on Ni foam applied as binder-free supercapacitor electrodes, *J. Energy Storage*, 2020, **32**, 101865.

4 R. K. Mishra, *et al.*, Vertical-slate-like MoS_2 nanostructures on 3D-Ni-foam for binder-free, low-cost, and scalable solid-state symmetric supercapacitors, *Curr. Appl. Phys.*, 2019, **19**(1), 1–7.

5 S. Gan, *et al.*, Electrochemically driven surface-confined acid/base reaction for an ultrafast H+ supercapacitor, *J. Am. Chem. Soc.*, 2016, **138**(5), 1490–1493.

6 S. Najib and E. Erdem, Current progress achieved in novel materials for supercapacitor electrodes: mini review, *Nanoscale Adv.*, 2019, **1**(8), 2817–2827.

7 T. Schoetz, *et al.*, Disentangling faradaic, pseudocapacitive, and capacitive charge storage: a tutorial for the characterization of batteries, supercapacitors, and hybrid systems, *Electrochim. Acta*, 2022, **412**, 140072.

8 P. Simon and Y. Gogotsi, Materials for electrochemical capacitors, *Nat. Mater.*, 2008, **7**(11), 845–854.

9 S. D. Dhas, *et al.*, Synthesis of NiO nanoparticles for supercapacitor application as an efficient electrode material, *Vacuum*, 2020, **181**, 109646.

10 J. Jayachandiran, *et al.*, Synthesis and electrochemical studies of rGO/ZnO nanocomposite for supercapacitor application, *J. Inorg. Org. Polym. Mater.*, 2018, **28**, 2046–2055.

11 H. Gao, *et al.*, Nanostructured spinel-type M (M= Mg, Co, Zn) Cr2O4 oxides: novel adsorbents for aqueous Congo red removal, *Mater. Today Chem.*, 2021, **22**, 100593.

12 Z.-A. Hu, *et al.*, Polyaniline/SnO_2 nanocomposite for supercapacitor applications., *Mater. Chem. Phys.*, 2009, **114**(2–3), 990–995.

13 S. Jayakumar, *et al.*, A comprehensive review of metal oxides (RuO_2, Co_3O_4, MnO_2 and NiO) for supercapacitor applications and global market trends., *J. Alloys Compd.*, 2024, **976**, 173170.

14 X. Hu, *et al.*, Reviews and Prospectives of Co_3O_4-Based Nanomaterials for Supercapacitor Application, *ChemistrySelect*, 2020, **5**(17), 5268–5288.

15 D. Majumdar, Review on current progress of MnO_2-based ternary nanocomposites for supercapacitor applications, *ChemElectroChem*, 2021, **8**(2), 291–336.

16 R. Bhujel, *et al.*, Electrochemical, bonding network and electrical properties of reduced graphene oxide-Fe_2O_3 nanocomposite for supercapacitor electrodes applications, *J. Alloys Compd.*, 2019, **792**, 250–259.

17 M. S. Javed, *et al.*, Exploring Li-ion hopping behavior in zinc ferrite and promoting performance for flexible solid-state supercapacitor, *Electrochim. Acta*, 2019, **295**, 558–568.

18 R. Devi, *et al.*, Arrangement of $ZnFe_2O_4$@PPy nanoparticles on carbon cloth for highly efficient symmetric supercapacitor, *J. Taiwan Inst. Chem. Eng.*, 2022, **138**, 104474.

19 F. Ozel, H. Kockar and O. Karaagac, Growth of iron oxide nanoparticles by hydrothermal process: effect of reaction parameters on the nanoparticle size, *J. Supercond. Novel Magn.*, 2015, **28**, 823–829.

20 N. Kandpal, *et al.*, Co-precipitation method of synthesis and characterization of iron oxide nanoparticles, *J. Sci. Ind. Res.*, 2014, 87–90.

21 G. Ennas, *et al.*, Characterization of iron oxide nanoparticles in an Fe_2O_3−SiO_2 composite prepared by a sol−gel method, *Chem. Mater.*, 1998, **10**(2), 495–502.

22 S. Kumar, *et al.*, Magnetic structure of Fe–Fe oxide nanoparticles made by electrodeposition, *Int. J. Eng., Sci. Technol.*, 2010, **2**(8), 66–72.

23 G. Ali, P. Yang Jeong, K. Jung Woo and C. Sung Oh, A green, general, and ultrafast route for the synthesis of diverse metal oxide nanoparticles with controllable sizes and enhanced catalytic activity, *ACS Appl. Nano Mater.*, 2018, **1**(11), 6112–6122.

24 S. Wienströer, *et al.*, Zinc/Iron phase transformation studies on galvannealed steel coatings by X-ray diffraction. International Centre for Diffraction, *Data*, 2003, **46**, 291–296.

25 S. Shrestha, B. Wang and P. Dutta, Nanoparticle processing: Understanding and controlling aggregation, *Adv. Colloid Interface Sci.*, 2020, **279**, 102162.

26 L. Kong, *et al.*, Electrochemically active sites inside crystalline porous materials for energy storage and conversion, *Chem. Soc. Rev.*, 2020, **49**(8), 2378–2407.

27 M. Sathyan, *et al.*, Electrode material for high performance symmetric supercapacitors based on superparamagnetic Fe_3O_4 nanoparticles modified with cetyltrimetylammonium bromide, *Synth. Metals*, 2022, **287**, 117080.

28 Q. Chen, *et al.*, Zn^{2+} pre-intercalation stabilizes the tunnel structure of MnO_2 nanowires and enables zinc-ion hybrid supercapacitor of battery-level energy density, *Small*, 2020, **16**(14), 2000091.

29 J. Halder, *et al.*, Bricks of Co, Ni doped Fe_3O_4 as high performing pseudocapacitor electrode, *J. Energy Storage*, 2023, **58**, 106391.

30 M. Sertkol, *et al.*, Synthesis and magnetic characterization of $Zn_{0.7}Ni_{0.3}Fe_2O_4$ nanoparticles via microwave-assisted combustion route, *J. Magn. Magn. Mater.*, 2010, **322**(7), 866–871.

31 S. Sobhanardakani, *et al.*, Removal of heavy metal (Hg (II) and Cr (VI)) ions from aqueous solutions using Fe_2O_3@ SiO_2 thin films as a novel adsorbent, *PProcess Saf. Environ. Prot.*, 2018, **120**, 348–357.

32 H. S. Chavan, *et al.*, Nanoflake $NiMoO_4$ based smart supercapacitor for intelligent power balance monitoring, *Solar Energy Mater. Solar Cells*, 2018, **185**, 166–173.

33 M. Najafi, *et al.*, Carbon-α-Fe_2O_3 composite active material for high-capacity electrodes with high mass loading and flat current collector for quasi-symmetric supercapacitors, *Electrochem*, 2022, **3**(3), 463–478.

34 L. Li, *et al.*, N-doped porous carbon-nanofiber-supported Fe_3C/Fe_2O_3 nanoparticles as anode for high-performance supercapacitors, *Molecules*, 2023, **28**(15), 5751.

35 Y. Dong, *et al.*, Porous α-Fe_2O_3@ C nanowire arrays as flexible supercapacitors electrode materials with excellent electrochemical performances, *Nanomaterials*, 2018, **8**(7), 487.

36 G. S. Gund, *et al.*, Low-cost flexible supercapacitors with high-energy density based on nanostructured MnO_2 and Fe_2O_3 thin films directly fabricated onto stainless steel, *Sci. Rep.*, 2015, **5**(1), 1–13.

37 L. Liu, *et al.*, Facile synthesis of Fe_2O_3 nano-dots@ nitrogen-doped graphene for supercapacitor electrode with ultralong cycle life in KOH electrolyte, *ACS Appl. Mater. Interfaces*, 2016, **8**(14), 9335–9344.

38 K. Xie, *et al.*, Highly ordered iron oxide nanotube arrays as electrodes for electrochemical energy storage, *Electrochem. Commun.*, 2011, **13**(6), 657–660.

39 P. Zhao, *et al.*, Facile hydrothermal fabrication of nitrogen-doped graphene/Fe_2O_3 composites as high performance electrode materials for supercapacitor, *J. Alloys Compd.*, 2014, **604**, 87–93.

40 H. Liu, *et al.*, Easy one-step hydrothermal synthesis of nitrogen-doped reduced graphene oxide/iron oxide hybrid as efficient supercapacitor material, *J. Solid State Electrochem.*, 2015, **19**, 135–144.

41 S. Shivakumara, T. R. Penki and N. Munichandraiah, Synthesis and characterization of porous flowerlike α-Fe_2O_3 nanostructures for supercapacitor application, *ECS Electrochem. Lett.*, 2013, **2**(7), A60.

42 S. Shivakumara, T. R. Penki and N. Munichandraiah, Preparation and electrochemical performance of porous hematite (α-Fe_2O_3) nanostructures as supercapacitor electrode material, *J. Solid State Electrochem.*, 2014, **18**, 1057–1066.